

Pd₂Se₃ Monolayer: A Promising Two Dimensional Thermoelectric Material with Ultralow Lattice Thermal Conductivity and High Power Factor

S. Shahab Naghavi,[†] Jiangan He,[‡] Yi Xia,[¶] and C. Wolverton[‡]

[†]*Department of Physical and Computational Chemistry, Shahid Beheshti University, G.C., Evin, 1983969411 Tehran, Iran*

[‡]*Department of Materials Science and Engineering, Northwestern University, Evanston, Illinois 60208, USA*

[¶]*Center for Nanoscale Materials, Argonne National Laboratory, 9700 South Cass Avenue, Lemont, Illinois 60439, United States*

Received April 19, 2018; E-mail:

Abstract: A high power factor and low lattice thermal conductivity are two essential ingredients of highly efficient thermoelectric materials. Although monolayers of transition metal dichalcogenides possess high power factors, high lattice thermal conductivities significantly impede their practical applications. Our first-principles calculations show that these two ingredients are well fulfilled in the recently synthesized Pd₂Se₃ monolayer, whose crystal structure is composed of [Se₂]²⁻ dimers, Se²⁻ anions, and Pd²⁺ cations coordinated in a square planar manner. Our detailed analysis of third-order interatomic force constants reveals that the anharmonicity and soft phonon modes associated with [Se₂]²⁻ dimers lead to ultra-low lattice thermal conductivities in Pd₂Se₃ monolayers (1.5 and 2.9 Wm⁻¹K⁻¹ along the *a*- and *b*-axes at 300 K respectively), which are comparable to those of high-performance bulk thermoelectric materials such as PbTe. Moreover, the “pudding-mold” type band structure, caused by Pd²⁺ (*d*⁸) cations coordinated in a square planar crystal field, leads to high power factors in Pd₂Se₃ monolayers. Consequently, both electron and hole doped thermoelectric materials with a considerably high *zT* can be achieved at moderate carrier concentrations, suggesting that Pd₂Se₃ is a promising two-dimensional thermoelectric material.

KEYWORDS: Pd₂Se₃ monolayer, thermoelectric, ultralow lattice thermal conductivity, pudding-mold band

Thermoelectric (TE) materials enable an environmentally friendly solution for direct and reversible conversion between heat and electricity. This two-way process has found increasing technological applications, such as solid-state refrigerators,¹ flat-panel solar thermoelectric generators,² space power, and recovery of waste heat.¹ Nevertheless, for a widespread use of TE materials, their efficiencies need to be significantly improved.³ The efficiency of TE materials is indexed by the dimensionless figure of merit $zT = S^2\sigma T/(\kappa_e + \kappa_L)$, where σ is electrical conductivity, S is thermopower or Seebeck coefficient, T is absolute temperature, κ_e and κ_L are respectively electrical and lattice thermal conductivities; $S^2\sigma$ is usually called power-factor (PF). An effective approach to improve zT is to reduce κ_L , either by searching for materials with intrinsically strong anharmonicity, or by enhancing phonon scattering by phonon engineering,⁴ e.g., nanostructuring.^{5–8} Likewise, another strategy is to enhance the PF by band structure engineering^{9–11} or finding a material with a desirable electronic structure, such as small band effective mass and high

valley degeneracy,⁹ or the flat-and-dispersive band structure^{12,13} (or pudding-mold band).^{12–16} In general, improving the electronic part (i.e., S , κ_e , and σ) is challenging: S and σ are generally inversely related¹⁷ and κ_e is proportional to σ (Wiedemann-Franz law). Therefore, improving the PF requires the tuning of three conflicting parameters, making the optimization of zT an extremely difficult task.

Alternatively, early theoretical work by Dresselhaus et al.^{18–20} and subsequent experimental work^{21–26} suggest that reducing the dimensionality of materials could significantly enhance zT . The quantum confinement effect in low dimensional materials significantly increases the density of electronic states, thus increasing PF, and their interfaces/surfaces can effectively scatter heat carrying phonons and thus suppressing κ_L . In fact, a simultaneous increase of S and reduction of κ_L has been observed in one-dimensional semiconducting materials (Bi₂Te₃ nanowires²⁴) and many two-dimensional (2D) semiconductors, such as phosphorene monolayers,²⁵ silicene,²⁶ and germanene.²⁶

In this context, transition-metal chalcogenide monolayers with nonzero band gaps have been intensively studied as promising candidates for 2D TE applications.^{27–43} In particular, transition-metal dichalcogenides (TMDCs) have been the focus of recent studies due to their large S .^{30–32} A previous study³⁰ found a remarkable enhancement of S in MoS₂ monolayers (30 mVK⁻¹) relative to the bulk phase (~ 7 mVK⁻¹). Despite improving S , a sizable zT has not been yet realized in TMDCs owing to their high κ_L ^{27–29,44} rooted in the covalent nature of bond between transition metal and chalcogenide atoms.^{45,46} The calculated κ_L of MoS₂, MoSe₂ and WSe₂, based on density functional theory (DFT), at 300 K are respectively 140, 80 and 40 Wm⁻¹K⁻¹,²⁸ which are in good agreement with the measured κ_L .

Transition-metal *tri*-chalcogenide (TMTCs) monolayers^{47–49} usually offer more complex atomic configurations and therefore more tortuous phonon paths⁴³ by incorporating both X₂²⁻ dimers and X²⁻ (X=S and Se) anions in their crystal structures. For instance, the κ_L of TiS₃⁴³ at 300 K (~ 10 Wm⁻¹K⁻¹) is much lower than that of WSe₂ (40 Wm⁻¹K⁻¹), even though both Ti and S atoms have much smaller atomic masses than W and Se. Nevertheless, such complex crystal structures are scarce in monolayers. Recently, Lin *et al.*⁵⁰ successfully synthesized a novel semiconducting Pd₂Se₃ monolayer with a unique crystal structure. The Pd₂Se₃ monolayer was synthesized by the fusion of two monolayers of PdS₂, though no Pd₂Se₃ bulk compound is yet reported. Due to the complex crystal structure ([Se₂]²⁻ and Se²⁻) and a large void in the monolayer, which

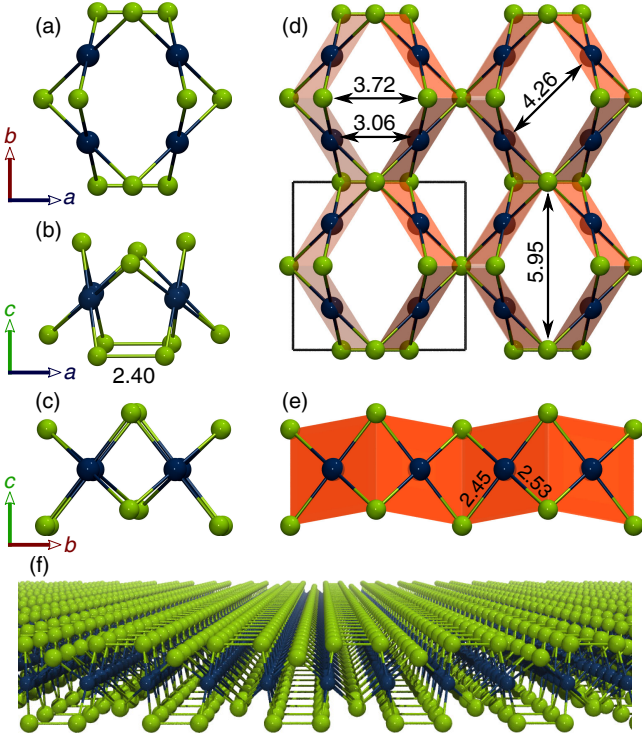


Figure 1. (a)–(f) Different views of monolayer Pd_2Se_3 structure. The square planar units are highlighted in orange.

is also not common among 2D materials, Pd_2Se_3 monolayers are expected to have a low κ_L . Moreover, the presence of pudding-mold type band structure^{12–15} could lead to a high PF in the Pd_2Se_3 monolayer.

In this work, we use first-principles DFT band structure, anharmonic phonon calculations, and Boltzmann transport theory,⁵¹ to provide a comprehensive study on the electronic and phonon transport properties of the Pd_2Se_3 monolayer. Our results show that Pd_2Se_3 monolayers have much lower κ_L and higher PF than all the previously reported transition-metal dichalcogenides²⁸ and trichalcogenides,⁴³ and thus possesses an overall better TE performance.

All the DFT calculations were performed using the projector-augmented wave (PAW) method^{52,53} as implemented in the Vienna Ab-initio Simulation Package (VASP).^{54,55} A plane wave basis set with energy cutoff of 350 eV and the generalized gradient approximation of Perdew-Burke-Ernzerhof (PBE)⁵⁶ to the exchange-correlation functional were used. A $12 \times 12 \times 1$ k -mesh is used to sample the first Brillouin zone. All structures were fully relaxed with respect to lattice vectors and atomic positions until the forces on each atom are less than $0.1 \text{ meV } \text{Å}^{-1}$. We found that the spin-orbit coupling (SOC) does not alter the dispersion of energy levels close to the Fermi level (see Figure S3) and therefore SOC was not included in our calculations. Electrical transport properties, i.e., S , σ and κ_e , were calculated using the Boltzmann transport theory within the constant relaxation time approximation as implemented in **BoltzTrap**.⁵⁷ The reciprocal space was sampled with a dense k -grid of $38 \times 38 \times 1$, to enable accurate Fourier interpolation of the Kohn-Sham eigenvalues. The κ_e was calculated using the Wiedemann-Franz law ($\kappa_e = L\sigma T$) with $L = 2.45 \times 10^{-8} \text{ W}\Omega\text{K}^{-2}$. Using the **ShengBTE** code,^{58–60} the κ_L is computed by solving the Boltzmann transport equation of phonons with the second- and third-order inter-

atomic force constants (IFCs) as input. The second-order IFCs were calculated by the **Phonopy** code⁶¹ using a $6 \times 6 \times 1$ supercell with $2 \times 2 \times 1$ k -point sampling. A $3 \times 3 \times 1$ supercell with $4 \times 4 \times 1$ k -point sampling was used to obtain third-order IFCs using **ShengBTE** code.^{58–60} A well-converged q -mesh ($30 \times 30 \times 1$) was used to calculate κ_L and related phonon properties.

Experimentally, Pd_2Se_3 monolayers have been synthesized by interlayer fusion of two defective PdSe_2 layers.⁵⁰ The monolayer is stable when exposed to air and at elevated temperatures.⁵⁰ Its crystal structure has an inversion center with the point group of $D_{2h} (mmm)$ and DFT calculated lattice parameters are 6.12 and 5.95 Å. As shown in Figure 1, the Pd atom has a square-planar coordination formed by $[\text{Se}_2]^{2-}$ and Se^{2-} . Such a coordination geometry is common among transition-metal complexes with the d^8 electronic configuration,^{12,16} suggesting that the oxidation state of Pd is 2+ in Pd_2Se_3 . Therefore, the coexistence of $[\text{Se}_2]^{2-}$ dimers and Se^{2-} anions leads to oxidation states of the stoichiometric compound as $[\text{Pd}^{2+}]_2[\text{Se}_2]^{2-}[\text{Se}_2]^{2-}$. The formation of $[\text{Se}_2]^{2-}$ dimers are supported by DFT calculated electron localization function (ELF) shown in Figure 4 (e), where the attractors (red area) on the midpoint of two selenide atoms indicate the covalent nature of bonding. The calculated Se–Se bond length of 2.4 Å (see Figure 1) is consistent with a fully oxidized two-center two-electron $[\text{Se}_2]^{2-}$ dimer.⁶² Therefore, there are two types of Pd–Se bonds in the Pd_2Se_3 monolayer: the longer Pd–Se bond formed between Pd^{2+} cation and Se^{2-} anion (2.53 Å) and the shorter one formed between Pd^{2+} and $[\text{Se}_2]^{2-}$ dimer (2.45 Å). The resulting crystal structure is thus complex with large rhombus-shape voids, as shown in Figure 1.

Slack’s theory⁶³ reveals that four factors lead to low κ_L : i) complex crystal structure, ii) high average mass, iii) weak interatomic bonding, and iv) anharmonicity. As will be discussed later, the complex crystal structure of Pd_2Se_3 features all those key characteristics, in particular, a strong anharmonicity stemming from the $[\text{Se}_2]^{2-}$ dimer.

Figure 2 (a) displays the phonon dispersion of the Pd_2Se_3 monolayer. The frequencies of all modes are positive in the whole Brillouin zone (BZ), implying that the Pd_2Se_3 monolayers are dynamically stable. The zone-boundary frequencies along Γ – X and Γ – Y are as low as 30 and 40 cm^{-1} . As seen in Figure 2, the acoustic bands, which play a dominant role in lattice heat transfer, have frequencies from 0 to 70 cm^{-1} , and are mainly localized on $[\text{Se}_2]^{2-}$ dimers and Pd^{2+} cations. Although Se^{2-} is light and its associated vibrations appear at high-frequency regions, the $[\text{Se}_2]^{2-}$ dimer acts like a heavy atom participating in low-frequency vibration modes.

The κ_L for each direction (i.e., a - and b -axes) is proportional to the square of the phonon group velocity along the respective direction.⁶⁵ The phonon group velocities of Pd_2Se_3 for the out-of-plane acoustic (ZA), transverse acoustic (TA), and longitudinal acoustic (LA) modes in the long-wavelength limit are listed in Table 1. The sound velocities of Pd_2Se_3 for all the acoustic branches are lower than those of MoS_2 and TiS_3 ,⁴³ suggesting a lower κ_L in the Pd_2Se_3 monolayer. On the other hand, the avoided crossing between the optical and acoustic modes is clearly seen in Figure 2 (a) along Γ – X and Γ – Y directions. The sizable gap at the avoided crossing point indicates a high coupling strength (hybridization) between optical and acoustic modes, which significantly increases the phonon scattering rates and re-

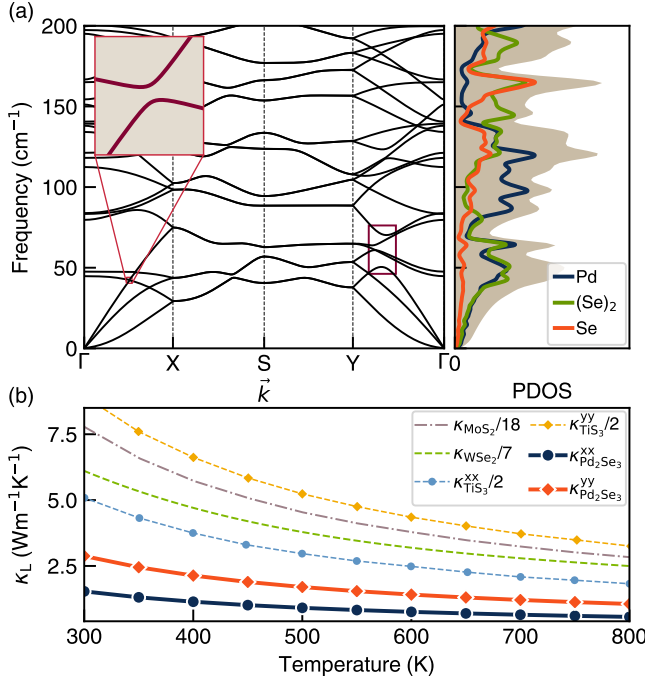


Figure 2. (a) Phonon dispersion and the density of states of Pd_2Se_3 with the highlighted avoided crossing bands. The density of states indicates that low-frequency modes are mainly composed of Se_2 dimers and heavy Pd atoms. (b) Calculated κ_L of Pd_2Se_3 compared to MoS_2 , WSe_2 and TiS_3 (notice that their κ_L is divided to an arbitrary number to fit into the figure window). The κ_L of Pd_2Se_3 is about 90, 27, 6 times lower than MoS_2 ,⁶⁴ WSe_2 ,²⁸ and TiS_3 ⁴³ respectively. The calculated κ_L of MoS_2 ,²⁸ which is not shown here, at $T=300$ K is about $80 \text{ Wm}^{-1}\text{K}^{-1}$. The atom projected κ_L (see Figure S9 in Supplementary Materials) indicates that Se_2 dimers and Pd atoms carry the most heat.

duces acoustic mode velocities, and thus leads to the low κ_L .

For the quantitative description of κ_L , we use first-principles calculations in conjunction with the self-consistent iterative solution of the Boltzmann transport equation (BTE) for phonons as implemented in *ShengBTE*.⁵⁸ The calculated κ_L as a function of temperature along the a - and b -directions are shown in Figure 2(b). The lattice thermal conductivity along the a (κ_L^{xx}) and b -axes (κ_L^{yy}) are 1.5 and $2.85 \text{ Wm}^{-1}\text{K}^{-1}$ at 300 K, respectively. They are comparable to those of high zT bulk materials such as PbTe , but much lower than other TMCs monolayers such as MoS_2 ($140 \text{ Wm}^{-1}\text{K}^{-1}$), TiS_3 ($10 \text{ Wm}^{-1}\text{K}^{-1}$), and WSe_2 ($42 \text{ Wm}^{-1}\text{K}^{-1}$). The calculated cumulative κ_L with respect to mean free path is shown in Figure S7. The result indicates that the κ_L can be further reduced by decreasing grain size of the polycrystal; for instance, at the size of 75 nm the κ_L^{xx} and κ_L^{yy} of the Pd_2Se_3 monolayer drop by 50% .

Table 1. Calculated group velocities of ZA, TA and LA phonons near the Γ point for the Pd_2Se_3 monolayer along the a - and b -direction compared with TiS_3 and MoS_2 .

Monolayer	Direction	ZA (Km/s)	TA(Km/s)	LA(km/s)
Pd_2Se_3	x	0.51	2.25	3.12
	y	0.50	2.27	3.19
TiS_3	x	0.88	3.01	5.43
	y	1.11	2.31	6.16
MoS_2	x, y	1.40	3.96	6.47

A comparison of κ_L for two selenide based TMCs mono-

layers, Pd_2Se_3 and WSe_2 , is illuminating. The atomic mass of the Pd (106.42) is much smaller than the W (183.4) and thus one might expect a higher κ_L for the Pd_2Se_3 . Nevertheless, as seen in Figure 2 the calculated κ_L of the Pd_2Se_3 monolayer is more than 20 times lower than WSe_2 . We next explore the origin of this behavior.

From the cumulative κ_L of phonon frequency (see Figure S8 in Supplementary Materials) we see that lattice heat transport is dominated by phonon modes with frequencies less than 80 cm^{-1} . In Figure 3 (a) and (b) we show the scattering rates associated with these low-lying phonon modes from three-phonon interactions, namely, the absorption ($\Gamma^+ : \lambda + \lambda' \rightarrow \lambda''$) and emission ($\Gamma^- : \lambda \rightarrow \lambda' + \lambda''$) processes. Different colors in the scattering rates plot show the scattering magnitude of the first phonon mode (λ) induced by the second phonon mode (λ'). In the absorption process, a low-frequency phonon mode contributes to other low-frequency optical modes, giving rise to a high-frequency optical mode. In the emission process, the phonon mode is only allowed to decompose into a lower-frequency mode, thus restricting the second phonon mode (λ') in the right lower triangle. Both processes satisfy energy and crystal-momentum conservation. Figure 3 (a) shows the strong scattering of acoustic modes through combination with low-lying optical modes ($\omega \approx 40 \text{ cm}^{-1}$), which is near the avoided crossing, consisting with high scattering rates due to avoided crossing bands. Phonon modes with frequencies ranging from 40 to 70 cm^{-1} , as shown in Figure 3 (a) and (b), are heavily scattered in both absorption and emission processes, indicating that the presence of low-lying optical modes significantly enhances overall phonon scattering rates.

To specify the role of each atom in the observed low κ_L , we calculate the atom projected κ_L , as shown in Figure S9 in Supplementary Materials. $[\text{Se}_2]^{2-}$ dimers and Pd^{2+} cation are largely responsible (90% in total) for heat transport in the Pd_2Se_3 monolayer, whereas the contribution of Se^{2-} is negligible. We also calculate the norm of third-order IFCs defined as $\Phi_{mnl} = \frac{\partial^3 E}{\partial u_m \partial u_n \partial u_l}$ (E and u are the total energy and atom displacement for different atom species m , n , and l). Since the phonon scattering rates are roughly proportional to $|\Phi|^2$,^{58,66} a high absolute value of Φ_{mnl} suggests a large anharmonicity. As shown in Figure 3(c), $\Phi_{\text{Se}_2\text{Se}_2\text{Se}_2}$ indicates a large anharmonicity associated with $[\text{Se}_2]^{2-}$ dimers, which is much higher than Pd^{2+} and Se^{2-} anions. Therefore, the low κ_L is a combined effect of strong anharmonic phonon-phonon interactions and small group velocities, stemming from the formation of $[\text{Se}_2]^{2-}$ dimers. This answers the question on why Pd_2Se_3 has a much lower κ_L than other TMCs, where such dimers do not form.

As already mentioned, in the Pd_2Se_3 monolayers the Pd^{2+} cation has a d^8 electronic configuration and a square planar crystal field, under which d orbitals split into four energy levels, d_{xz}/d_{yz} , d_{z^2} , d_{xy} , and $d_{x^2+y^2}$ from low to high energy. On the other hand, the packing of square planar units in the crystal lattice induces a weak interaction between the nearby Pd^{2+} cations, separated by 3.06 \AA , via d_{z^2} orbitals as seen in Figure 4 (c). This interaction switches the energy levels of d_{z^2} with d_{xy} (see Figure S1 in Supplementary Materials). Note that in the Pd_2Se_3 monolayers, the d_{z^2} orbital almost lies along the a -axis. Due to the strong crystal field splitting associated with square planar geometry, the low spin state is always preferred in Pd^{2+} . As a result, the four low-energy levels are occupied by the eight electrons of Pd^{2+} (d^8) cations, where the d_{z^2} is the highest occupied orbitals (the

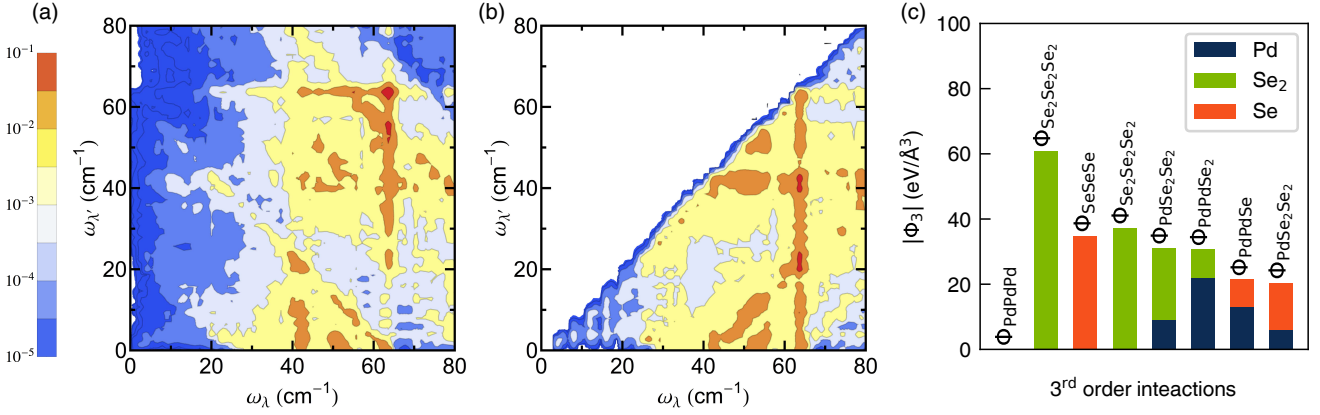


Figure 3. Contour plot of phonon scattering rate of the first phonon mode λ induced by the second phonon mode λ' in the three phonon processes, namely, absorption (a) and emission (b) processes in which crystal momentum and energy are conserved. (c) Norm of the calculated third-order interatomic force constants, indicating the magnitude of anharmonicity.

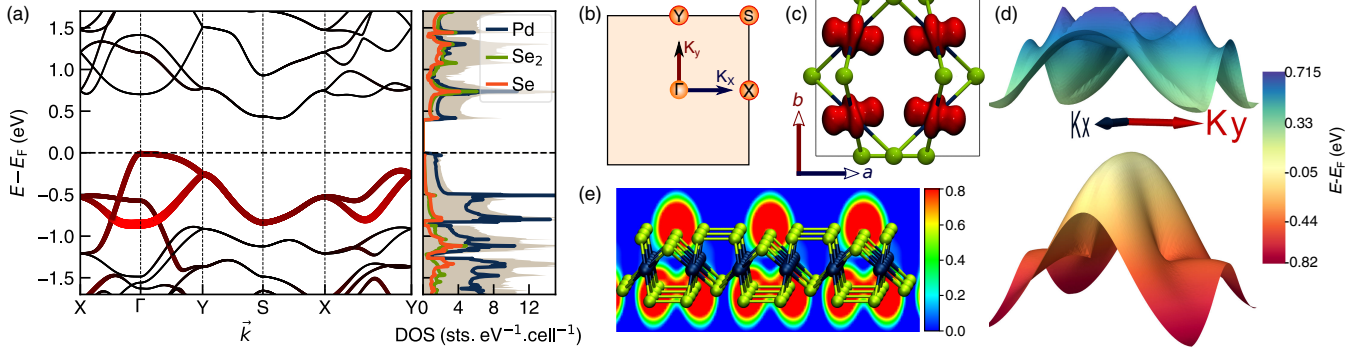


Figure 4. (a) DFT (PBE) orbital projected band structure (line width and red color correspond to the contribution of Pd-4d₂ orbitals) and projected density of states (PDOS). (b) Schematic Brillouin zone, (c) decomposed charge density of the top of the valence band, (e) electron localization function (ELF) viewed along b -axis, and (d) three dimensional band structure of Pd₂Se₃.

top of the valence band). Therefore the Pd₂Se₃ monolayer is a band insulator, in which the top of the valence band is mainly composed of d_{z^2} orbital, as seen in Figure 4 (a), and the bottom of the conduction band is largely from $d_{x^2+y^2}$ (see Figure S2).

As the overlap of d_{z^2} orbital with the p_x and p_y orbitals of the nearest anion is negligible, a relatively flat band along the b -axis is expected. As seen in Figure 4 (a) and (b), the valence band maximum along the $\Gamma - Y$ is relatively flat, affording a high density of states (DOS) near the Fermi level. On the other hand, a proper overlap between Pd²⁺ d_{z^2} orbitals along the a -axis leads to a very dispersive band along the $X - \Gamma$ direction, indicating a small band effective mass and therefore high carrier mobility. This type of band structure, known as the flat-and-dispersive or “pudding-mold” type band structure, has been found in high-performance bulk TE materials¹⁶ such as Na_{*x*}CoO₂,^{14,15} Bi₂PdO₄,¹² and some full Heusler compounds.^{13,67} This actually coincides with the idea proposed by Mahan and Sofo⁶⁶ that “*we have to search for materials where the distribution of energy carriers is as narrow as possible, but with high carrier velocity in the direction of the applied electric field.*”. A highly dispersive band (small band effective mass) around the Fermi level gives rise to a large σ , while a sharp increase in the density of states owing to the presence of a flat band (large band effective mass) usually leads to a large S .⁶⁶ In the case of the Pd₂Se₃ monolayers, the calculated effective masses (m^*) for holes along the dispersive band is about 0.17 m_0 and for

the flat band is 9.14 m_0 , thus a high S and σ are expected along the a -axis.

In Figure 5, we plot the calculated electronic transport coefficients for hole (p -type) and electron (n -type) doped Pd₂Se₃ monolayers at varying temperatures. The calculated PF along the a -axis for both p -type and n -type systems, assuming $\tau = 1 \times 10^{-14}$ s and $T=300$ K, are respectively 1.61 and 1.29 mW/mK². Along the b -axis, while the PF of n -type is large (0.7 mW/mK²), the p -type is quite small (0.1 mW/mK²). Thus, a large PF anisotropy is established with a dominant PF along the a -axis in the p -type Pd₂Se₃ monolayers. Using the same electronic relaxation time, the maximum PF for MoS₂, MoSe₂, WSe₂, and TiS₃ at the same temperature are ≈ 1.8 mW/mK² (n -type),⁶⁸ 0.8 mW/mK² (n -type),²⁸ 1.7 mW/mK² (n -type)²⁸ and 1.8 mW/mK² (n -type),⁴³ respectively. The PF of Pd₂Se₃ monolayers, 1.61 mW/mK² (p -type) and 1.21 mW/mK² (n -type), is comparable to these TMCs, while its κ_L is one to two orders of magnitudes lower (see Figure 2). Therefore, a larger zT for the Pd₂Se₃ monolayers is expected.

In Figure 5 we calculate the zT at the varying relaxation times within a reasonable range⁶⁹ from 5 to 55×10^{-15} s. The zT of p -type Pd₂Se₃ monolayers along the a -axis is about 16% larger than the n -type one. Depending on the relaxation time the calculated n -type zT values vary between 0.15 to ≈ 1 . Along b -axis, a large difference between n - and p -type zT values is found. Using the same τ , our calculated zT values are much larger than the previously reported TMCs

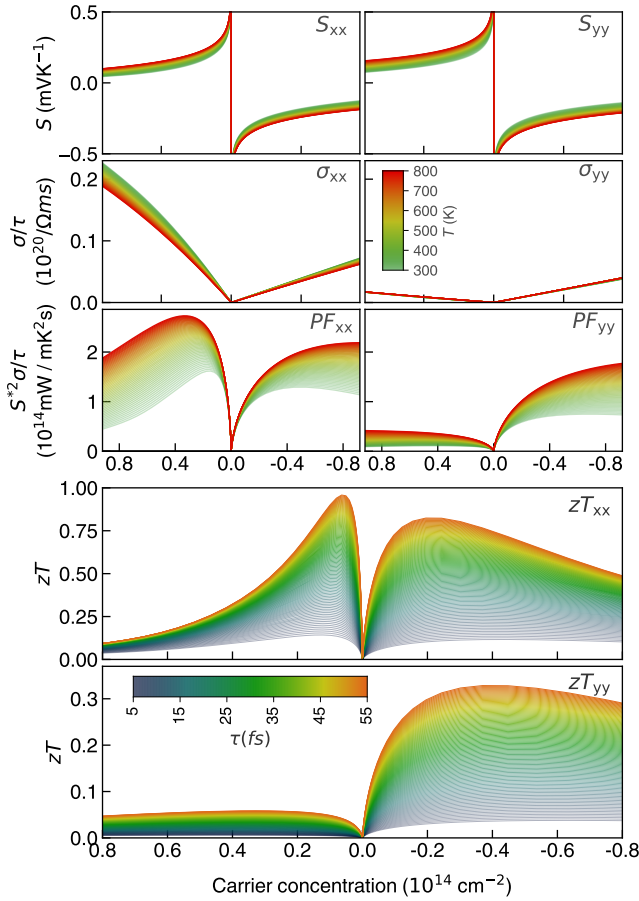


Figure 5. The calculated transport coefficients (PF, S , σ) and zT of Pd_2Se_3 as a function of carrier concentrations with respectively various temperatures and electron relaxation time (τ) at 300 K.

such as TiS_3 ,⁴³ MoSe_2 , WSe_2 ,²⁸ PtSe_2 .²⁹ Our calculations suggest that Pd_2Se_3 monolayers are promising TE material in both n -type and p -type applications.

In conclusion, we investigated the electronic structure, phonon, and electron and phonon transport properties of the recently synthesized Pd_2Se_3 monolayers by the means of first-principles calculations and Boltzmann transport theory. Our results demonstrate that the Pd_2Se_3 monolayers possess a much lower lattice thermal conductivity than other TMC monolayers, e.g., MoS_2 , MoSe_2 , WSe_2 , Ti_2Se_3 . Detailed analysis of third-order force constants indicates that the anharmonicity and soft phonon modes associated with $[\text{Se}_2]^{2-}$ dimers are responsible for the low lattice thermal conductivity of Pd_2Se_3 . On the other hand, the “pudding-mold” type band structure, originating from the square-planar coordinated Pd^{2+} cation, offers a high power factor. An extremely low lattice thermal conductivity in conjunction with a high power factor leads, of course, to the superior TE performance in the Pd_2Se_3 monolayer. Our results suggest the Pd_2Se_3 monolayer is a promising two-dimensional thermoelectric material with a high zT for both hole and electron doping.

ACKNOWLEDGMENTS

J. H. and C. W. (electronic structure, thermoelectric calculations and analysis) acknowledge support by the U.S. Department of Energy, Office of Science and Office of Basic Energy

Sciences, under Award No. DE-SC0014520. Y.X (analysis of phonon calculations) acknowledges the Center for Nanoscale Materials, an Office of Science user facility, supported by the U. S. Department of Energy, Office of Science, Office of Basic Energy Sciences, under Contract No. DE-AC02-06CH11357. The authors acknowledge computing resources provided on Blues, a high-performance computing cluster operated by the Laboratory Computing Resource Center at Argonne National Laboratory.

References

- (1) Rowe, D. M. *CRC handbook of thermoelectrics*; CRC press, 1995.
- (2) Kraemer, D.; Poudel, B.; Feng, H.-P.; Caylor, J. C.; Yu, B.; Yan, X.; Ma, Y.; Wang, X.; Wang, D.; Muto, A.; McEnaney, K.; Chiesa, M.; Ren, Z.; Chen, G. High-performance flat-panel solar thermoelectric generators with high thermal concentration. *Nat Mater* **2011**, *10*, 532–538.
- (3) Snyder, G. J.; Toberer, E. S. Complex thermoelectric materials. *Nat Mater* **2008**, *7*, 105–114.
- (4) Toberer, E. S.; Zevalkink, A.; Snyder, G. J. Phonon engineering through crystal chemistry. *J. Mater. Chem.* **2011**, *21*, 15843–15852.
- (5) Majumdar, A. Thermoelectricity in Semiconductor Nanostructures. *Science* **2004**, *303*, 777–778.
- (6) Xie, W.; Weidenkaff, A.; Tang, X.; Zhang, Q.; Poon, J.; Tritt, T. Recent Advances in Nanostructured Thermoelectric Half-Heusler Compounds. *Nanomaterials* **2012**, *2*, 379–412.
- (7) Poudel, B.; Hao, Q.; Ma, Y.; Lan, Y.; Minnich, A.; Yu, B.; Yan, X.; Wang, D.; Muto, A.; Vashaee, D.; Chen, X.; Liu, J.; Dresselhaus, M. S.; Chen, G.; Ren, Z. High-Thermoelectric Performance of Nanostructured Bismuth Antimony Telluride Bulk Alloys. *Science* **2008**, *320*, 634–638.
- (8) Biswas, K.; He, J.; Blum, I. D.; Chun-IWu, Hogan, T. P.; Seidman, D. N.; Dravid, V. P.; Kanatzidis, M. G. Corrigendum: High-performance bulk thermoelectrics with all-scale hierarchical architectures. *Nature* **2012**, *490*, 570–570.
- (9) Pei, Y.; Shi, X.; LaLonde, A.; Wang, H.; Chen, L.; Snyder, G. J. Convergence of electronic bands for high performance bulk thermoelectrics. *Nature* **2011**, *473*, 66–69.
- (10) Liu, W.; Tan, X.; Yin, K.; Liu, H.; Tang, X.; Shi, J.; Zhang, Q.; Uher, C. Convergence of Conduction Bands as a Means of Enhancing Thermoelectric Performance of n -Type $\text{Mg}_2\text{Si}_{1-x}\text{Sn}_x$ Solid Solutions. *Phys. Rev. Lett.* **2012**, *108*, 166601.
- (11) Yu, B.; Zebarjadi, M.; Wang, H.; Lukas, K.; Wang, H.; Wang, D.; Opeil, C.; Dresselhaus, M.; Chen, G.; Ren, Z. Enhancement of thermoelectric properties by modulation-doping in silicon germanium alloy nanocomposites. *Nano Lett.* **2012**, *12*, 2077–2082.
- (12) He, J.; Hao, S.; Xia, Y.; Naghavi, S. S.; Ozoliš, V.; Wolverton, C. Bi_2PdO_4 : A Promising Thermoelectric Oxide with High Power Factor and Low Lattice Thermal Conductivity. *Chem. Mater.* **2017**, *29*, 2529–2534.
- (13) Bilc, D. I.; Hautier, G.; Waroquiers, D.; Rignanese, G.-M.; Ghosez, P. Low-Dimensional Transport and Large Thermoelectric Power Factors in Bulk Semiconductors by Band Engineering of Highly Directional Electronic States. *Phys. Rev. Lett.* **2015**, *114*, 136601.
- (14) Usui, H.; Kuroki, K. Enhanced power factor and reduced Lorenz number in the Wiedemann-Franz law due to pudding mold type band structures. *Journal of Applied Physics* **2017**, *121*, 165101.
- (15) Kuroki, K.; Arita, R. Pudding Mold Band Drives Large Thermopower in Na_xCoO_2 . *J. Phys. Soc. Japan* **2007**, *76*, 083707.
- (16) Isaacs, E. B.; Wolverton, C. Inverse Band Structure Design via Materials Database Screening: Application to Square Planar Thermoelectrics. *Chemistry of Materials* **2018**.
- (17) Mateeva, N.; Niculescu, H.; Schlenoff, J.; Testardi, L. R. Correlation of Seebeck coefficient and electric conductivity in polyaniline and polypyrrole. *J. Appl. Phys.* **1998**, *83*, 3111–3117.
- (18) Hicks, L. D.; Dresselhaus, M. S. Thermoelectric figure of merit of a one-dimensional conductor. *Phys. Rev. B* **1993**, *47*, 16631–16634.
- (19) Dresselhaus, M. S.; Dresselhaus, G.; Sun, X.; Zhang, Z.; Cronin, S. B.; Koga, T. Low-dimensional thermoelectric materials. *Phys. Solid State* **1999**, *41*, 679–682.
- (20) Dresselhaus, M. S.; Chen, G.; Tang, M. Y.; Yang, R.; Lee, H.; Wang, D.; Ren, Z.; Fleurial, J.-P.; Gogna, P. New directions for low-dimensional thermoelectric materials. *Advanced materials* **2007**, *19*, 1043–1053.
- (21) Harman, T. C. Quantum Dot Superlattice Thermoelectric Materials and Devices. *Science* **2002**, *297*, 2229–2232.
- (22) Venkatasubramanian, R.; Siivola, E.; Colpitts, T.; O’Quinn, B. Thin-film thermoelectric devices with high room-temperature figures of merit. *Nature* **2001**, *413*, 597–602.
- (23) Hochbaum, A. I.; Chen, R.; Delgado, R. D.; Liang, W.; Garnett, E. C.; Najarian, M.; Majumdar, A.; Yang, P. Enhanced thermoelectric performance of rough silicon nanowires. *Nature* **2008**, *451*, 163–167.

- (24) Zhang, G.; Kirk, B.; Jauregui, L. A.; Yang, H.; Xu, X.; Chen, Y. P.; Wu, Y. Rational Synthesis of Ultrathin n-Type Bi₂Te₃ Nanowires with Enhanced Thermoelectric Properties. *Nano Lett.* **2012**, *12*, 56–60.
- (25) Fei, R.; Faghaninia, A.; Soklaski, R.; Yan, J.-A.; Lo, C.; Yang, L. Enhanced Thermoelectric Efficiency via Orthogonal Electrical and Thermal Conductances in Phosphorene. *Nano Lett.* **2014**, *14*, 6393–6399.
- (26) Yang, K.; Cahangirov, S.; Cantarero, A.; Rubio, A.; D'Agosta, R. Thermoelectric properties of atomically thin silicene and germanene nanostructures. *Phys. Rev. B* **2014**, *89*, 125403.
- (27) Huang, W.; Da, H.; Liang, G. Thermoelectric performance of MX₂ (M Mo,W; X S,Se) monolayers. *J. Appl. Phys.* **2013**, *113*, 104304.
- (28) Kumar, S.; Schwingenschlög, U. Thermoelectric Response of Bulk and Monolayer MoSe₂ and WSe₂. *Chem. Mater.* **2015**, *27*, 1278–1284.
- (29) Guo, S.-D. Biaxial strain tuned thermoelectric properties in monolayer PtSe₂. *J. Mater. Chem. C* **2016**, *4*, 9366–9374.
- (30) Wu, J.; Schmidt, H.; Amara, K. K.; Xu, X.; Eda, G.; Özyilmaz, B. Large thermoelectricity via variable range hopping in chemical vapor deposition grown single-layer MoS₂. *Nano Lett.* **2014**, *14*, 2730–2734.
- (31) Yoshida, M.; Iizuka, T.; Saito, Y.; Onga, M.; Suzuki, R.; Zhang, Y.; Iwasa, Y.; Shimizu, S. Gate-Optimized Thermoelectric Power Factor in Ultrathin WSe₂ Single Crystals. *Nano Lett.* **2016**, *16*, 2061–2065.
- (32) Buscema, M.; Barkelid, M.; Zwiller, V.; van der Zant, H. S. J.; Steele, G. A.; Castellanos-Gomez, A. Large and Tunable Photothermoelectric Effect in Single-Layer MoS₂. *Nano Lett.* **2013**, *13*, 358–363.
- (33) Li, W.; Carrete, J.; Mingo, N. Thermal conductivity and phonon linewidths of monolayer MoS₂ from first principles. *Appl. Phys. Lett.* **2013**, *103*, 253103.
- (34) Guo, S.-D. Strain effect on power factor in monolayer MoS₂. *Comput. Mater. Sci.* **2016**, *123*, 8–13.
- (35) Ding, G.; Gao, G. Y.; Huang, Z.; Zhang, W.; Yao, K. Thermoelectric properties of monolayer MSe₂ (M = Zr, Hf): low lattice thermal conductivity and a promising figure of merit. *Nanotechnology* **2016**, *27*, 375703.
- (36) Guo, S. D.; Wang, Y. H. Thermoelectric properties of orthorhombic group IV-VI monolayers from the first-principles calculations. *J. Appl. Phys.* **2017**, *121*, 034302.
- (37) Shafique, A.; Shin, Y.-H. Thermoelectric and phonon transport properties of two-dimensional IVVI compounds. *Sci. Rep.* **2017**, *7*, 506.
- (38) Jin, Z.; Liao, Q.; Fang, H.; Liu, Z.; Liu, W.; Ding, Z.; Luo, T.; Yang, N. A Revisit to High Thermoelectric Performance of Single-layer MoS₂. *Sci. Rep.* **2016**, *5*, 18342.
- (39) Sun, J.; Shi, H.; Siegrist, T.; Singh, D. J. Electronic, transport, and optical properties of bulk and mono-layer PdSe₂. *Appl. Phys. Lett.* **2015**, *107*, 2–6.
- (40) Wang, J.; Xie, F.; Cao, X.-H.; An, S.-C.; Zhou, W.-X.; Tang, L.-M.; Chen, K.-Q. Excellent Thermoelectric Properties in monolayer WSe₂ Nanoribbons due to Ultralow Phonon Thermal Conductivity. *Sci. Rep.* **2017**, *7*, 41418.
- (41) Wang, Y.; Li, Y.; Chen, Z. Not your familiar two dimensional transition metal disulfide: structural and electronic properties of the PdS₂ monolayer. *J. Mater. Chem. C* **2015**, *3*, 9603–9608.
- (42) Zhang, Z.; Xie, Y.; Peng, Q.; Chen, Y. A theoretical prediction of super high-performance thermoelectric materials based on MoS₂/WS₂ hybrid nanoribbons. *Sci. Rep.* **2016**, *6*, 21639.
- (43) Zhang, J.; Liu, X.; Wen, Y.; Shi, L.; Chen, R.; Liu, H.; Shan, B. Titanium Trisulfide Monolayer as a Potential Thermoelectric Material: A First-Principles-Based Boltzmann Transport Study. *ACS Appl. Mater. Interfaces* **2017**, *9*, 2509–2515.
- (44) Peng, B.; Zhang, H.; Shao, H.; Xu, Y.; Zhang, X.; Zhu, H. Thermal conductivity of monolayer MoS₂, MoSe₂, and WS₂: interplay of mass effect, interatomic bonding and anharmonicity. *RSC Adv.* **2016**, *6*, 5767–5773.
- (45) Chhowalla, M.; Shin, H. S.; Eda, G.; Li, L.-J.; Loh, K. P.; Zhang, H. The chemistry of two-dimensional layered transition metal dichalcogenide nanosheets. *Nat. Chem.* **2013**, *5*, 263–275.
- (46) Yun, W. S.; Han, S. W.; Hong, S. C.; Kim, I. G.; Lee, J. D. Thickness and strain effects on electronic structures of transition metal dichalcogenides: 2H-MX₂ semiconductors (M = Mo, W; X = S, Se, Te). *Phys. Rev. B* **2012**, *85*, 033305.
- (47) Island, J. O.; Buscema, M.; Barawi, M.; Clamagirand, J. M.; Ares, J. R.; Sánchez, C.; Ferrer, I. J.; Steele, G. A.; van der Zant, H. S.; Castellanos-Gomez, A. Ultrahigh photoresponse of few-layer TiS₃ nanoribbon transistors. *Adv. Opt. Mater.* **2014**, *2*, 641–645.
- (48) Lipatov, A.; Wilson, P.; Shekhirev, M.; Teeter, J.; Netusil, R.; Sinitksii, A. Few-layered titanium trisulfide (TiS₃) field-effect transistors. *Nanoscale* **2015**, *7*, 12291–12296.
- (49) Pawbake, A. S.; Island, J. O.; Flores, E.; Ares, J. R.; Sanchez, C.; Ferrer, I. J.; Jadkar, S. R.; Van Der Zant, H. S.; Castellanos-Gomez, A.; Late, D. J. Temperature-Dependent Raman Spectroscopy of Titanium Trisulfide (TiS₃) Nanoribbons and Nanosheets. *ACS Appl. Mater. Interfaces* **2015**, *7*, 24185–24190.
- (50) Lin, J.; Zuluaga, S.; Yu, P.; Liu, Z.; Pantelides, S. T.; Suenaga, K. Novel Pd₂Se₃ Two-Dimensional Phase Driven by Interlayer Fusion in Layered PdSe₂. *Phys. Rev. Lett.* **2017**, *119*, 016101.
- (51) Allen, P. Boltzmann theory and resistivity of metals. *KLUWER INTERNATIONAL SERIES IN ENGINEERING AND COMPUTER SCIENCE* **1996**, 219–250.
- (52) Blöchl, P. E. Projector augmented-wave method. *Phys. Rev. B* **1994**, *50*, 17953–17979.
- (53) Kresse, G.; Joubert, D. From ultrasoft pseudopotentials to the projector augmented-wave method. *Phys. Rev. B* **1999**, *59*, 1758–1775.
- (54) Kresse, G.; Furthmüller, J. Efficient iterative schemes for *ab-initio* total-energy calculations using a plane-wave basis set. *Phys. Rev. B* **1996**, *54*, 11169–11186.
- (55) Kresse, G.; Furthmüller, J. Efficiency of *ab-initio* total energy calculations for metals and semiconductors using a plane-wave basis set. *Comput. Mater. Sci.* **1996**, *6*, 15–50.
- (56) Perdew, J. P.; Burke, K.; Ernzerhof, M. Generalized Gradient Approximation Made Simple. *Phys. Rev. Lett.* **1997**, *78*, 1396–1399.
- (57) Madsen, G. K.; Singh, D. J. BoltzTraP. A code for calculating band-structure dependent quantities. *Computer Physics Communications* **2006**, *175*, 67–71.
- (58) Li, W.; Carrete, J.; Katcho, N. A.; Mingo, N. ShengBTE: a solver of the Boltzmann transport equation for phonons. *Comp. Phys. Commun.* **2014**, *185*, 17471758.
- (59) Li, W.; Mingo, N.; Lindsay, L.; Broido, D. A.; Stewart, D. A.; Katcho, N. A. Thermal conductivity of diamond nanowires from first principles. *Phys. Rev. B* **2012**, *85*, 195436.
- (60) Li, W.; Lindsay, L.; Broido, D. A.; Stewart, D. A.; Mingo, N. Thermal conductivity of bulk and nanowire Mg₂Si_xSn_{1-x} alloys from first principles. *Phys. Rev. B* **2012**, *86*, 174307.
- (61) Togo, A.; Oba, F.; Tanaka, I. First-principles calculations of the ferroelastic transition between rutile-type and CaCl₂-type SiO₂ at high pressures. *Phys. Rev. B* **2008**, *78*, 134106.
- (62) O'Keeffe, M.; Brese, N. E. Bond-valence parameters for anion-anion bonds in solids. *Acta Crystallogr. Sect. B Struct. Sci.* **1992**, *48*, 152–154.
- (63) Slack, G. Nonmetallic crystals with high thermal conductivity. *J. Phys. Chem. Solids* **1973**, *34*, 321–335.
- (64) Gandi, A. N.; Schwingenschlög, U. Thermal conductivity of bulk and monolayer MoS₂. *EPL (Europhysics Lett.)* **2016**, *113*, 36002.
- (65) Mingo, N.; Stewart, D.; Broido, D.; Lindsay, L.; Li, W. *Length-Scale Dependent Phonon Interactions*; Springer, 2014; pp 137–173.
- (66) Mahan, G. D.; Sofo, J. O. The best thermoelectric. *Proc. Natl. Acad. Sci.* **1996**, *93*, 7436–7439.
- (67) He, J.; Amsler, M.; Xia, Y.; Naghavi, S. S.; Hegde, V. I.; Hao, S.; Goedecker, S.; Ozoliš, V.; Wolverson, C. Ultralow thermal conductivity in full Heusler semiconductors. *Physical review letters* **2016**, *117*, 046602.
- (68) Babaei, H.; Khodadadi, J. M.; Sinha, S. Large theoretical thermoelectric power factor of suspended single-layer MoS₂. *Appl. Phys. Lett.* **2014**, *105*, 193901.
- (69) González-Romero, R. L.; Antonelli, A.; Meléndez, J. J. Insights into the thermoelectric properties of SnSe from *ab initio* calculations. *Phys. Chem. Chem. Phys.* **2017**, *19*, 12804–12815.